ACS OMEGA

http://pubs.acs.org/journal/acsodf

Article

Multifunctional Lanthanide-Doped Binary Fluorides and Graphene Oxide Nanocomposites Via a Task-Specific Ionic Liquid

Rahul Kumar Sharma, Madhubrata Ghora, Yogendra N. Chouryal, Trisit Ganguly, Debopam Acharjee, Dibya Jyoti Mondal, Sanjit Konar, Sandeep Nigam, and Pushpal Ghosh*

Cite This: *ACS Omega* 2022, 7, 16906−16916

Read Online

ACCESS | Metrics & More | Article Recommendations | Supporting Information

ABSTRACT: Graphene oxide-based nanocomposites (NCMs) exhibit diverse photonic and biophotonic applications. Innovative nanoengineering using a task-specific ionic liquid (IL), namely, 1-butyl-3-methyl tetrafluoroborate [C_4mim][BF_4], allows one to access a unique class of luminescent nanocomposites formed between lanthanide-doped binary fluorides and graphene oxide (GO). Here the IL is used as a solvent, templating agent, and as a reaction partner for the nanocomposite synthesis, that is, "all three in one". Our study shows that GO controls the size of the NCMs; however, it can tune the luminescence properties too. For example, the excitation spectrum of Ce^{3+} is higher-energy shifted when GO is attached. In addition, magnetic properties of GdF_3:Tb^{3+} nanoparticles (NPs) and GdF_3:Tb^{3+}-GO NCMs are also studied at room temperature (300 K) and very low temperature (2 K). High magnetization results for the NPs (e.g., 6.676 emu g^{-1} at 300 K and 184.449 emu g^{-1} at 2 K in the applied magnetic field from +50 to −50 kOe) and NCMs promises their uses in many photonic and biphotonic applications including magnetic resonance imaging, etc.

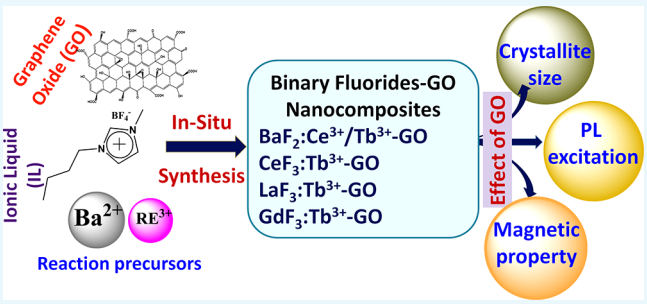

1. INTRODUCTION

Graphene oxide (GO) and inorganic- or organic-based nanocomposite materials (NCMs) have drawn a center of curiosity due to their widespread applications in optoelectronics, batteries, catalysis, photocatalysis, magnetism, bioimaging, solar cells, etc.[1−15] Normally, making a composite between two different materials enables one to obtain a property combination that may not be available from a single material.[11,15−18] Graphene oxide is obtained by the oxidation and subsequent exfoliation of graphite via a chemical route. Graphene is fundamentally one atom thick and two-dimensional (2D) with a honeycomb-like structure that was discovered by Novoselov et al. in 2004.[19] Since then, it has been attracting tremendous attention in nanoscience and nanotechnology. However, rare-earth (RE^{3+})-doped binary/ternary fluorides and GO-based nanocomposite materials are very limitedly studied. Commonly, nanocomposite materials are lanthanide oxides and GO nanocomposites (Ln = Ce and Gd), GO doped with RE ions, and lanthanide-based metallo-organic frameworks (MOFs) attached with GO, etc.[13,15,20−27] However, RE^{3+}-doped fluorides with GO nanocomposite are still in their infancy. Currently, a very limited number of rare-earth fluorides and graphene oxide nanocomposite materials are explored including upconverting $NaYF_4$ doped with Yb, Er/Tm nanoparticles (NPs).[12−15,28,29] There are numerous approaches for the synthesis of graphene, graphene oxide, and derivatives of GO-based nanocomposite materials. Among them, hydrothermal and solvothermal methods are frequently being used for the synthesis of inorganic nanomaterials and GO-based composite nanomaterials.[15,30,31] In this perspective, inorganic nanomaterials synthesis using task-specific ionic liquids (ILs) are paving a new way due to their interesting and tunable features. Normally ILs are comprised of highly tunable organic cation and organic/inorganic anion combinations with a melting point less than 100 °C in ambient conditions.[32] ILs are often considered as *green and designer* solvents in various applications including nanomaterials synthesis.[33,34] However, with a judicious selection of the cation and anion combinations, physical and chemical properties of ILs can be tuned, which can influence nanomaterials synthesis.[32,34−41] The intricate properties of ILs allow them to serve as a reaction medium, capping/templating agent, and reaction partner, sometimes "all three in one".[32,34−41] For example, ILs containing tetrafluoroborate (BF_4^-), hexafluorophosphate (PF_6^-), and dihydrogenphospate ($H_2PO_4^-$) anions as counter-ions have been used for an in situ synthesis of fluoride- and phosphate-based RE^{3+}-doped nanoparticles, respectively.[39−42]

Received: December 5, 2021
Accepted: April 27, 2022
Published: May 11, 2022

ACS Publications

© 2022 The Authors. Published by American Chemical Society

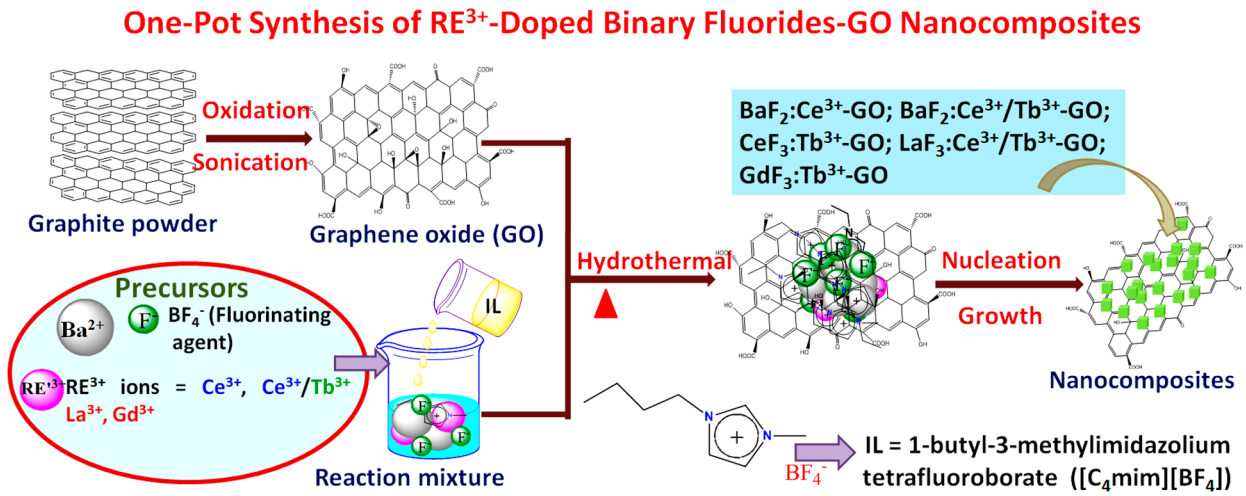

Figure 1. Schematic representation of the synthesis method of nanocomposites using the IL that is $[C_4mim][BF_4]$ to assist via a hydrothermal method.

Table 1. Phase, Crystallite Size, and Lattice Strain of As-Prepared RE^{3+}-Doped Binary Fluorides Nanoparticles and Nanocomposites (with Graphene Oxide, GO)

code	sample name	IL	crystal phase	crystallite size (nm)	avg strain (η%)	lattice strain
M1	$BaF_2:Ce^{3+}$	yes	cubic	92.3	−0.35	compressive
M2	$BaF_2:Ce^{3+}/Tb^{3+}$	yes	cubic	100.7	−0.10	compressive
M3	$BaF_2:Ce^{3+}$-GO	yes	cubic	82.1	−0.24	compressive
M4	$BaF_2:Ce^{3+}/Tb^{3+}$-GO	yes	cubic	81.5	−0.22	compressive
M5	$LaF_3:Ce^{3+}/Tb^{3+}$	yes	hexagonal	32.6	0.49	tensile
M6	$CeF_3:Tb^{3+}$	yes	hexagonal	38.6	0.29	tensile
M7	$GdF_3:Tb^{3+}$	yes	orthorhombic	24.0	1.38	tensile
M8	$LaF_3:Ce^{3+}/Tb^{3+}$-GO	yes	hexagonal	29.2	0.54	tensile
M9	$CeF_3:Tb^{3+}$-GO	yes	hexagonal	20.0	0.62	tensile
M10	$GdF_3:Tb^{3+}$-GO	yes	orthorhombic	22.7	0.23	tensile

Besides this, tunable properties of ILs have been used to control the crystal phase, size, and morphology to stabilize nanoparticles, particularly metallic nanoparticles, etc.[34−38,40]

Herein, we synthesized RE^{3+} (Ce or Tb or Ce/Tb)-doped binary fluorides with GO nanocomposites (NCMs) using a 1-butyl-3-methyl tetrafluoroborate $[C_4mim][BF_4]$ IL-assisted hydrothermal method, where the IL not only acts as a solvent and templating agent but is also employed as a fluoride source, that is, all three in one (Figure 1 and Table 1). Here, an environmentally benign and "green" method is adopted in which only water and $[C_4mim][BF_4]$ IL are used. Water is only employed with an IL to facilitate the hydrolysis of the BF_4^- anion for readily releasing the F^- ions (For details of the synthesis/characterization of pure GO, nanomaterials, nanocomposites, etc., see the Supporting Information). In this way, the IL is used in a one-pot synthesis route in which all the reacting precursors are put simultaneously under the similar reaction conditions ($[C_4mim][BF_4]$ IL, 6 h and 150 °C) via the hydrothermal method for the preparation of RE^{3+} (Ce^{3+}, Tb^{3+}, or Ce^{3+}/Tb^{3+})-doped binary fluoride nanoparticles such as $BaF_2:Ce^{3+}$(M1), $BaF_2:Ce^{3+}/Tb^{3+}$(M2), $LaF_3:Ce^{3+}/Tb^{3+}$(M5), $CeF_3:Tb^{3+}$(M6), and $GdF_3:Tb^{3+}$(M7) and their nanocomposites with GO like $BaF_2:Ce^{3+}$-GO (M3), $BaF_2:Ce^{3+}/Tb^{3+}$-GO (M4), $LaF_3:Ce^{3+}/Tb^{3+}$-GO (M8), $CeF_3:Tb^{3+}$-GO (M9), and $GdF_3:Tb^{3+}$-GO (M10) (Figure 1). In addition, the role of GO in the crystallite size, morphology, and excitation and emission spectra of RE^{3+}-doped nanoparticles is also studied. From an application point of view, the magnetization of Gd^{3+}-doped NPs and NCMs is also measured.

2. EXPERIMENTAL SECTION

2.1. Chemicals. Details and the purity of the chemicals used are given in the Supporting Information.

2.2. Synthesis of $[C_4mim][Br]$ IL. By modifying a previously reported method, 1-butyl-3-methylimidazolium bromide $[C_4mim][Br]$ was synthesized by adding the 0.166 mol of 1-bromobutane dropwise to stirring (0.126 mol) 1-methyl imidazole over 30 min at 0 °C in a 250 mL round-bottom flask.[43] Then the round-bottom flask was covered with aluminum foil, and the reaction proceeded at room temperature for 96 h. After the reaction was completed, the obtained product was washed with ethyl acetate and stirred for 1 h. The obtained product was dried in vacuum for 12 h to get a white solid crystal. This white crystalline product can be further used for the preparation of $[C_4mim][BF_4]$IL.

Synthesis of $[C_4mim][BF_4]$ IL. The room-temperature ionic liquid (RTIL) $[C_4mim][BF_4]$ was prepared by adding $NaBF_4$ (21 g) and 1-butyl-3-methylimidazolium bromide $[C_4mim]$-[Br] (42 g) in acetone (100 mL) and allowing this to stir at room temperature (RT) for 3−4 d.[41,44] The obtained product was filtered and then stirred continually for further 16 h with 1 g of activated charcoal. The activated charcoal was filtered, and acetone was finally removed by a rotary evaporator under vacuum. The obtained product was further mixed with ∼60

https://doi.org/10.1021/acsomega.1c06875
ACS Omega 2022, 7, 16906−16916

mL of dichloromethane (at least three to four times) to make it free from impurities. A little amount of silver nitrate solution was added to the washed ionic liquid to confirm the chloride ions. The pale yellowish liquid was isolated and further dried in a vacuum for 12 h. Details of ^{1}H and ^{13}C NMR spectra are given in the Supporting Information.

2.3. Synthesis of Graphene Oxide (GO). Details of the synthesis of graphene oxide and its characterization through powder X-ray diffraction (PXRD) and Raman spectra are given in the Supporting Information (Figure S1 and Figure S2).

2.4. Synthesis of BaF_2:RE^{3+} (Ce^{3+}) NPs. In the present work, binary fluoride is used as a material both for nanoparticles and nanocomposites. A good "host" for efficient doping of rare-earth ions and its luminescence must adhere the following criteria: it should have low phonon energy, high refractive index, tunable crystal phase, etc. In the present case, binary fluorides like BaF_2, LaF_3, CeF_3, GdF_3, etc. all follow those prerequisites mentioned and are used as host materials.

1% Ce^{3+}-doped BaF_2 NPs are typically synthesized by a reported method.[41] Separately, 2.5 mL of aqueous solutions of barium acetate (2.8 mmol) and cerium nitrate were stirred for 5 min in separate beakers. The barium acetate and cerium nitrate solutions were mixed. Then, 4.5 mL of $[C_4mim][BF_4]$ IL was added to the barium acetate and cerium nitrate solution, and this was stirred for 5 min followed by the addition of 10 mL of DI water. Then the reaction mixture was transferred to a 100 mL Teflon-lined autoclave with a stainless steel jacket and kept inside the hot air oven for 6 h at 150 °C. And then the obtained product was washed several times with methanol, ethanol, and acetone and then dried at 60 °C overnight. Other products such as BaF_2:Ce^{3+}/Tb^{3+}, CeF_3:Tb^{3+}, LaF_3:Ce^{3+}/Tb^{3+}, and GdF_3:Tb^{3+} were also synthesized using a similar procedure.

2.5. One Pot Synthesis of BaF_2:RE^{3+}(RE = Ce^{3+})-GO NCMs. 50 mg of GO was added in 10 mL of DI water and sonicated for 30 min (Steps 1 and 2 in Figure 2). Thereafter, 2.5 mL aqueous solutions of barium acetate (2.8 mmol) and cerium nitrate were stirred for 5 min in separate beakers (Steps 3 and 4). The barium acetate and cerium nitrate solutions were mixed. Then, 4.5 mL of $[C_4mim][BF_4]$ IL (Step 5) was added to the barium acetate and cerium nitrate solution, which was stirred continually for 5 min leading to form a reaction mixture (Step 6 of Figure 2). GO solution (10 mL) was added to the above solution and stirred for 5 min (Step 7 of Figure 2). Then the reaction mixture was transferred to a 100 mL Teflon-lined autoclave with a stainless steel jacket and kept inside the hot air oven for 6 h at 150 °C. And then the obtained product was washed several times with methanol, ethanol, and acetone and then dried at 60 °C overnight (Step 8 of Figure 2). Using the aforementioned synthesis protocol, other products, such as BaF_2:Ce^{3+}/Tb^{3+}-GO and CeF_3:Tb^{3+}-GO, LaF_3:Ce^{3+}/Tb^{3+}-GO and GdF_3:Tb^{3+}-GO, etc., were also synthesized (Figures 1 and 2). In this work, Ce^{3+} works mainly as a sensitizer and Tb^{3+} ion as an activator. Reduction of GO during synthesis of NCMs was confirmed using Fourier transform infrared (FTIR) spectra (as shown in Figure S3).

2.6. Characterizations. Powder X-ray diffraction (PXRD) data of the samples were obtained with a D8 Advance Bruker, equipped with Cu Kα (1.540 60 Å) as the incident radiation. The morphology of the as-prepared nanoparticles and nanocomposites was measured using the field-emission scanning electron microscopy (FESEM) of NOVA NanoSEM 450 and transmission electron microscopy (TEM) of FEI Tecnai G2 20 S-Twin, 200 kV. The atomistic level growth of nanoparticles and nanocomposites was confirmed using high-resolution (HR) TEM. The FTIR measurement was performed using a Bruker Tensor 37. Photoluminescence (PL) spectra were recorded using a Horiba Jobin Yvon Fluoromax-4 spectrofluorometer. Raman spectra were measured using a Renishaw via a Raman microscope. Nuclear magnetic resonance spectrometry (JEOL Bruker ECX 500 (500 MHz)) was used for measuring NMR spectra in $CDCl_3$. The magnetization measurement was performed using a Quantum Design SQUID-VSM magnetometer at 2 and 300 K.

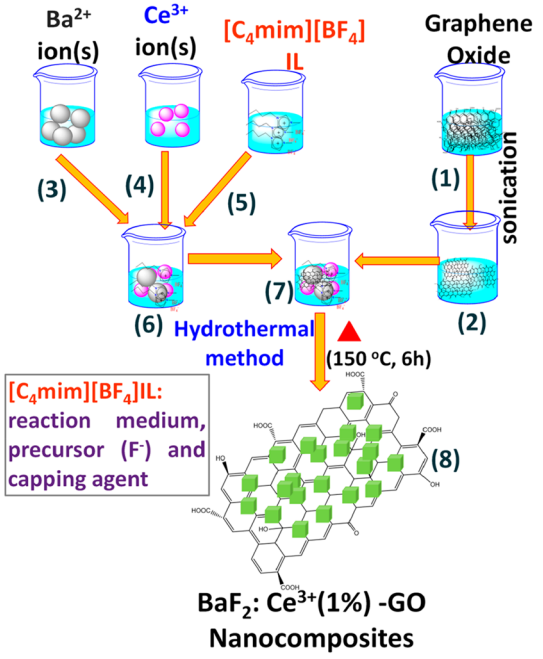

Figure 2. Schematic representation of the synthesis method of BaF_2:Ce^{3+}-GO nanocomposites using $[C_4mim][BF_4]$ IL-assisted via a hydrothermal method.

3. RESULTS AND DISCUSSION

3.1. Structural Characterization by Powder X-ray Diffraction (PXRD). The PXRD patterns of the as-synthesized phase-pure cubic BaF_2 NPs and NCMs doped with Ce^{3+} and Ce^{3+}/Tb^{3+} nicely matches with JCPDS card No. C4-452 (Figure S4(i)). Additionally, PXRD patterns of other Ln-based NPs and NCMs match with JCPDS card Nos. C32-483 (LaF_3), C8-45 (CeF_3), and C12-788 (GdF_3), respectively (Figure 3a and Figure S4(ia)). No extra peak due to any impurity or dopant ion(s) is noticed. The crystallite size of RE^{3+}-doped BaF_2 NPs is also measured with and without GO (Table 1). Interestingly, the crystallite size of BaF_2:RE^{3+}(1%) NPs is found bigger and significantly diverse in the absence of GO than that of with GO. In the absence of GO, crystallite sizes are 92.3 and 100.7 nm for BaF_2:Ce^{3+} and BaF_2:Ce^{3+}/Tb^{3+} NPs, respectively. However, when GO is employed to synthesize the NCMs according to Figures 1 and 2, a smaller size of Ce^{3+} or Ce^{3+}/Tb^{3+}-doped BaF_2 NPs is found. For example, 81.5 and 82.1 nm are obtained for Ce^{3+}/Tb^{3+} and Ce^{3+}-doped BaF_2-GOs NCMs, respectively (Table 1). Likewise, for other Ln-based NPs and their NCMs, a significant change in the crystallite size of NPs compared to NCMs is found. For instance, in the absence of GO, the crystallite size of LaF_3:Ce^{3+}/Tb^{3+}, CeF_3:Tb^{3+}, and GdF_3:Tb^{3+} corresponds to

https://doi.org/10.1021/acsomega.1c06875
ACS Omega 2022, 7, 16906−16916

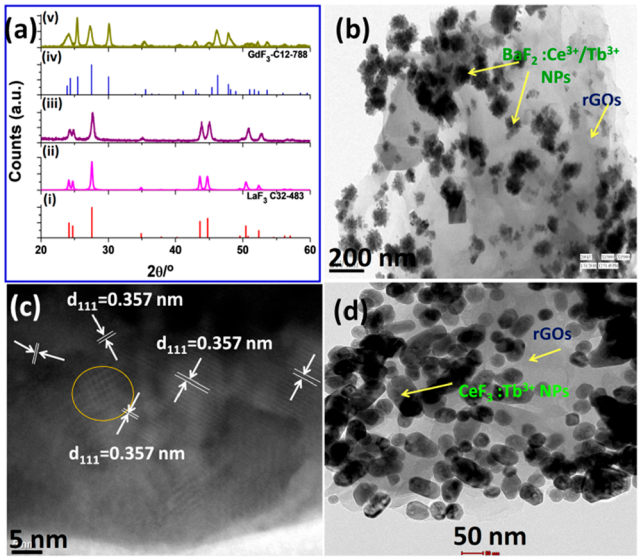

Figure 3. (a) PXRD patterns: (i) LaF_3 standard, (ii) LaF_3:Ce^{3+}/Tb^{3+}-GO (M8), (iii) CeF_3:Tb^{3+}-GO (M9), (iv) GdF_3 standard, (v) GdF_3:Tb^{3+}-GO (M10). (b) Low-magnification TEM image of BaF_2:Ce^{3+}-GO NCMs, (c) HRTEM image BaF_2:Ce^{3+}/Tb^{3+}-GO NCMs, and (d) low-magnification TEM image of CeF_3:Tb^{3+}-GO NCMs formed by one-pot synthesis using the $[C_4mim][BF_4]$ IL-assisted hydrothermal method.

32.6, 38.6, and 24.0 nm, respectively (Table 1). However, when these nanoparticles are prepared in situ with GO as a nanocomposite, the sizes of NPs are noticeably reduced to 29.2, 20.0, and 22.7 nm for LaF_3:Ce^{3+}/Tb^{3+}-GO, CeF_3:Tb^{3+}-GO, and GdF_3:Tb^{3+}-GO, respectively (Table 1). Thus, the crystallite size of NPs is substantially reduced in the presence of GO indicating the role of GO itself as a capping agent.

3.2. Lattice Strain. Commonly, the nature of diffraction peaks of particles can be related to the crystallite size and lattice strain. Therefore, the lattice strain and crystallite size can be determined by the equation of Williamson and Hall[41]

$$\frac{\beta\cos\theta}{\lambda} = \frac{1}{D} + \eta\frac{\sin\theta}{\lambda}$$

where η is the effective strain, D is the crystallite size, and λ is the X-ray wavelength. When we plot $\beta\cos\theta/\lambda$ versus $\sin\theta/\lambda$, the strain can be derived from the slope. The positive and negative magnitudes of the slope indicate the tensile and compressive strains, respectively.

The lattice strain of NPs and NCMs are determined using the Williamson-Hall equation as mentioned above. The compressive strain is observed for BaF_2:Ce^{3+} and BaF_2:Ce^{3+}/Tb^{3+} binary fluorides in the presence and absence of GO (Figures 4(i)). Interestingly, the magnitude of the compressive strain is found very close for BaF_2:Ce^{3+}-GO (−0.24%) and BaF_2:Ce^{3+}/Tb^{3+}-GO NCMs (−0.22%) (Figure 4(i)a,b). However, in the case of bare BaF_2:Ce^{3+} and BaF_2:Ce^{3+}/Tb^{3+} NPs, compressive strain is found to be −0.35% and −0.1%, respectively (Figure 4(ii)a,b). This can be attributed to having an approximately similar crystallite size of (BaF_2:Ce^{3+} and BaF_2:Ce^{3+}/Tb^{3+}) NPs in the presence of GO (Table 1). However, in the case of CeF_3:Tb^{3+}, LaF_3:Ce^{3+}/Tb^{3+}, and GdF_3:Tb^{3+} NPs and their NCMs with GO, only tensile strain is found. The significant influence of GO on the magnitude of tensile strain is noticed. For instance, 0.49%, 0.29%, and 1.38% tensile strains are found for LaF_3:Ce^{3+}/Tb^{3+}, CeF_3:Tb^{3+}, and GdF_3:Tb^{3+} NPs in the absence of GO, respectively (Figure 4(ii)c−e). Unlike the other two, on incorporating the GO to form NCMs, tensile strain is noticeably reduced to 0.23% for GdF_3:Tb^{3+}-GO NCMs (shown in Figure 4(i)e).

3.3. Structural Characterizations by Scanning Electron Microscope (SEM) and Transmission Electron Microscope (TEM). The morphology of the as-prepared GO, NPs, and NCMs is depicted using the FESEM and TEM images (see Figures 3b−d, 5, and S5−S7). In the case of RE^{3+} (Ce^{3+} and Ce^{3+}/Tb^{3+})-doped BaF_2 NPs and their NCMs counterpart, agglomerated, small spherical or oval-shaped along with a bigger size and cubic/cubical morphology of particles are found (Figures 3b). LaF_3:Ce^{3+}/Tb^{3+}, CeF_3:Tb^{3+}, and GdF_3:Tb^{3+} NPs and their respective NCMs are also prepared using GO under the similar reaction condition. The

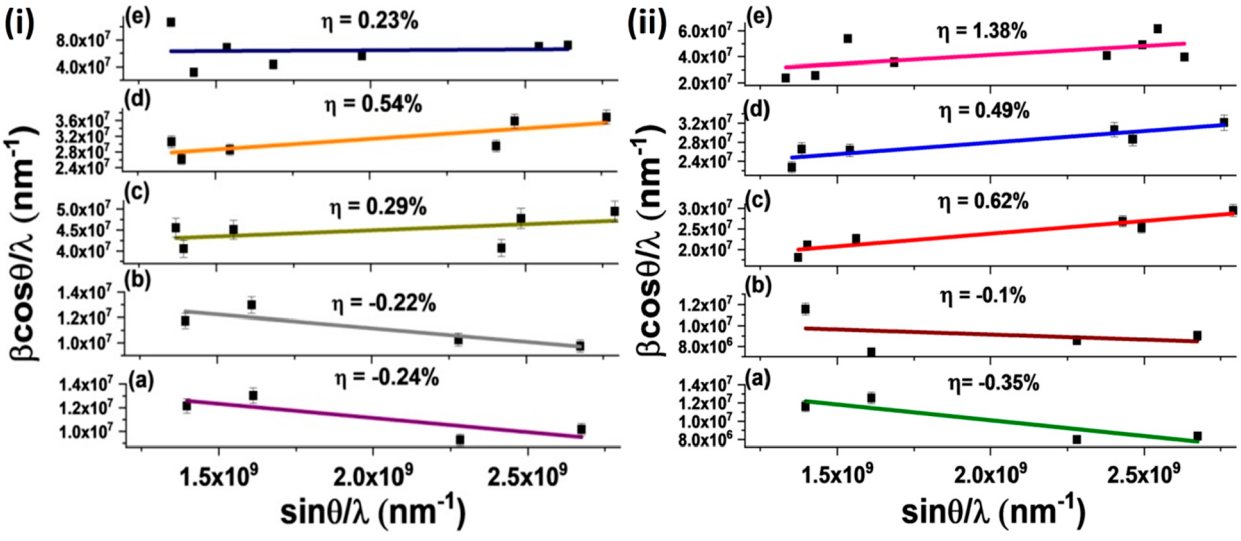

Figure 4. Lattice strain of NCMs: (i) (a) BaF_2:Ce^{3+}-GO, (b) BaF_2:Ce^{3+}/Tb^{3+}-GO, (c) CeF_3:Tb^{3+}-GO, (d) LaF_3:Ce^{3+}/Tb^{3+}-GO, (e) GdF_3:Tb^{3+}-GO; (ii) (a) BaF_2:Ce^{3+}; (b) BaF_2:Ce^{3+}/Tb^{3+}; (c) CeF_3:Tb^{3+}; (d) LaF_3:Ce^{3+}/Tb^{3+}; (e) GdF_3:Tb^{3+} synthesized using the $[C_4mim][BF_4]$ IL-assisted hydrothermal method.

https://doi.org/10.1021/acsomega.1c06875
ACS Omega 2022, 7, 16906−16916

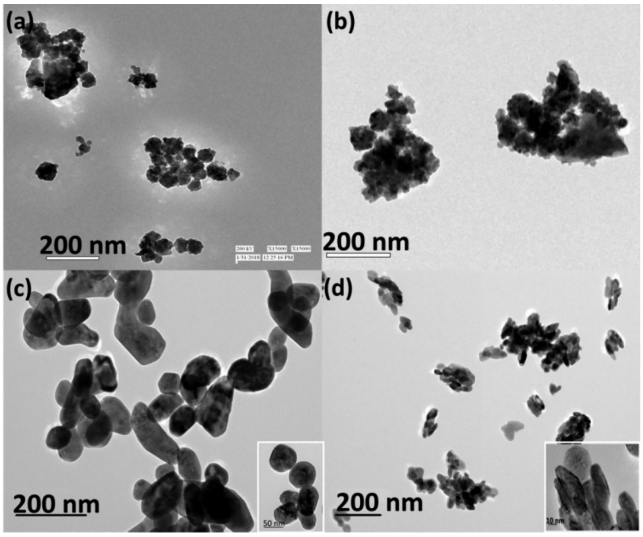

Figure 5. TEM images of as-prepared RE^{3+}(1%)-doped binary fluoride NPs. (a) BaF_2:Ce^{3+}, (b) BaF_2:Ce^{3+}/Tb^{3+}, (c) LaF_3:Ce^{3+}/Tb^{3+}, and (d) GdF_3:Tb^{3+}, synthesized using the $[C_4mim][BF_4]$ IL-assisted hydrothermal method.

morphology of LaF_3:Ce^{3+}/Tb^{3+} and CeF_3:Tb^{3+} NPs are found to be spherical-shaped (Figures 3d, 5c, and S6a). However, TEM images reveal that a mixed morphology is obtained for as-prepared LaF_3:Ce^{3+}/Tb^{3+} NPs and CeF_3:Tb^{3+} NPs, in which small NPs are oval-shaped while matured NPs have the elongated hexagonal shape (Figures 3d, 5c, and S6a). However, GdF_3:Tb^{3+} NPs and its NCMs with GO have completely different morphology, that is, spindle-shaped (in Figures 5d and S6b), and it seems to be made of small NPs. Thus, an analysis reveals that the morphology is dependent on the nature of the precursor ions used for the synthesis of the host matrix and also illustrated earlier.[45] For understanding the growth mechanism from the atomistic level and to confirm NCMs formation, HRTEM images are taken. HRTEM images of as-prepared BaF_2:Ce^{3+}/Tb^{3+}(1%)-GOs NCMs reveal that the growth of NPs is preferentially taking place along the (111) plane, which corresponds to *d*-spacing of ∼0.357 nm (Figure 3c). The formation of cubic-shaped NPs is basically due to the isotropic growth of particles along the (111) dominant plane. Besides, Moiré patterns (highlighted by a yellow circle) are also appearing due to the overlapping of two similar planes having comparable energy (Figure 3c). From TEM images, it is clear that NPs are distributed onto the GO surface almost homogeneously (according to Figure 3). The attachment of NPs on the surface of GO is attributed to the electrostatic attraction between GO and NPs, which leads to the formation of NCMs (Figures 3b,d and S7b).[17] This synthesis strategy has shown that RE^{3+} ion-doped BaF_2/LnF_3-GO NCMs can be effortlessly synthesized at moderate temperature using IL.

It is worth mentioning that, even though the lanthanide-doped binary fluorides (BaF_2, CeF_3, LaF_3, GdF_3) have different crystal structures (Figure 6), the ionic liquid 1-butyl-3-methyl tetrafluoroborate $[C_4mim][BF_4]$ is able to facilitate the synthesis of nanoparticles and nanocomposites with graphene oxide (GO). This may be attributed to the involvement of the ionic liquid at a microscopic level/atomic level in controlling the reaction and facilitating the formation of a metal−fluorine bond under a different crystallographic symmetry.

It is known that ILs act as a reaction partner, solvent, and capping/templating agent. On the one hand, an anionic part like BF_4^-, $H_2PO_4^-$, Br^-, I^-, etc. of ILs acts as a source of reaction partner, and the anionic (BF_4^-, $H_2PO_4^-$) part of the IL is decomposed into F^- and PO_4^{3-} in the presence of water. On the other hand, the cationic part (imidazolium, pyridinium, ammonium, ions, etc.) participates in the capping/templating agent.[46−48] For example, Zheng et al. have shown that the

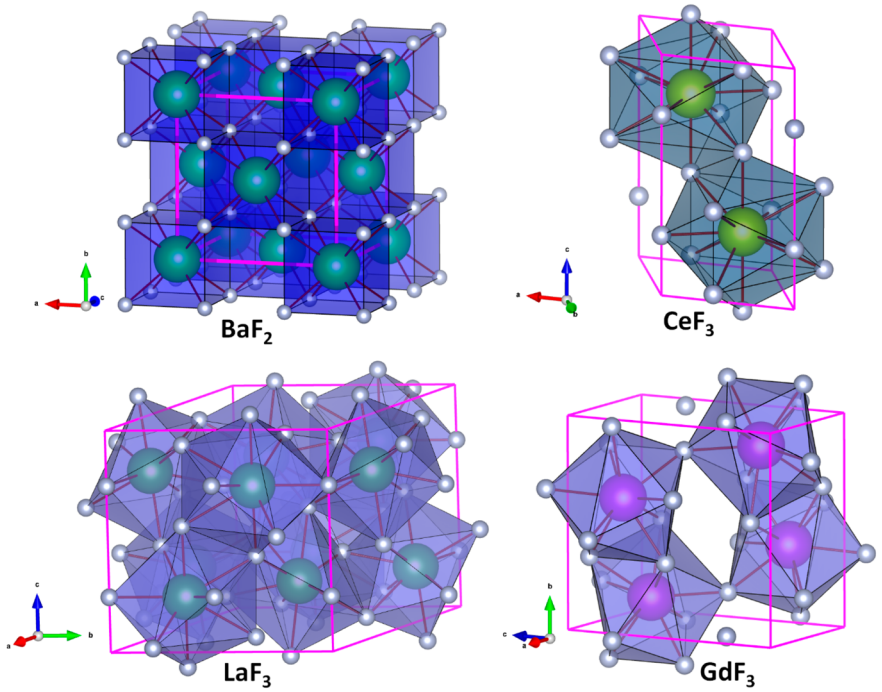

Figure 6. Representative crystal structures of BaF_2 [*Fm*3*m* (cubic)], CeF_3 [*P*63/*mcm* (hexagonal)], LaF_3 [$P\bar{3}c1$ (hexagonal)], and GdF_3 [*Pnma* (orthorhombic)].

https://doi.org/10.1021/acsomega.1c06875
ACS Omega 2022, 7, 16906−16916

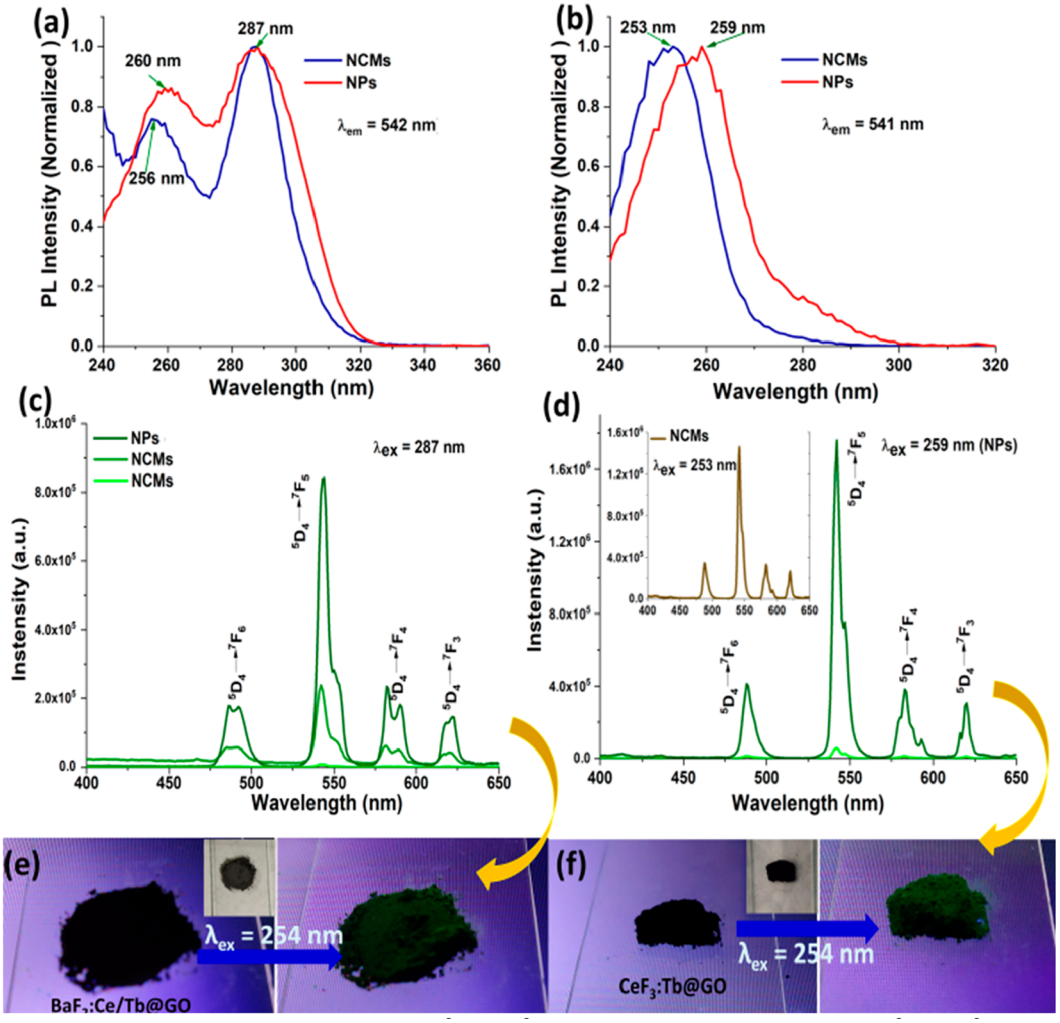

Figure 7. PL excitation spectra: (a) BaF_2:Ce^{3+}/Tb^{3+} NPs (M2) and BaF_2:Ce^{3+}/Tb^{3+}-GO NCMs (M4), (b) CeF_3:Tb^{3+} NPs (M6) and CeF_3:Tb^{3+}-GO NCMs (M9). PL emission spectra: (c) BaF_2:Ce^{3+}/Tb^{3+} NPs (M2) and BaF_2:Ce^{3+}/Tb^{3+}-GO NCMs (M4) and (d) CeF_3:Tb^{3+} NPs (M6) and CeF_3:Tb^{3+}-GO NCMs (M9), inset shows emission of NCMs (M9) at higher slit width and measured at RT, (e, f) BaF_2:Ce^{3+}/Tb^{3+}-GO and CeF_3:Tb^{3+}-GO NCMs are illuminated using UV lamp (6 W).

$[Emim]^+$ ions can serve as capping agents based on their strong interactions with the (110) facets of rutile, and the [Emim]Br favors the formation of the rutile structure with a rod-like shape due to the mutual π-stacking interactions of imidazole rings.[48] It has been experimentally as well as theoretically proven that the cationic moiety of an IL is self-assembled about the nucleation site during the growth of nanoparticles. And by binding at the particular facet of nanoparticles, an IL governed the growth of nanoparticles.[48−51] Wu et al. synthesized $BaY_{0.78}F_5$:$Yb_{0.7}$,$Tm_{0.02}$ upconverting nanoparticles in which $NaBF_4$ is used as a source of fluoride (F^-) ion and ethylenediaminetetraacetic acid (EDTA) as a surface active agent.[52] Thereafter, as-prepared nanoparticles are functionalized with other moieties (tetraethyl orthosilicate (TEOS), (3-aminopropyl)triethoxysilane (APTES), avidin, etc.) in order to bind the nanoparticles with a graphene oxide surface for desired applications. Similarly, Malik et al. discloses the incorporation of graphene quantum dots (GQDs) on the growth of β-$NaYF_4$:Gd^{3+}/Tb^{3+} phosphor crystals via a hydrothermal route.[53] The GQDs function as a nucleation site, and by changing the concentration of GQDs, the morphology of β-$NaYF_4$:Gd^{3+}/Tb^{3+} phosphors was changed from a rod to flowerlike to disklike structure, without a phase transformation. Likewise, Wei et al. synthesized GO−$NaYF_4$:Yb/Er nanocomposites in the water/ethanol (1:1, v/v) solution.[14] And then they have studied the optical limiting property of GO−$NaYF_4$:Yb/Er nanocomposites. During synthesis, sodium fluoride (NaF) and ethanol are used as a source of fluoride ion and cosolvent, respectively. They have also reported that the luminescence of nanoparticles is significantly quenched in the presence of GO.

In the present work, the nanocomposites are prepared by a one-pot process using an ionic liquid-assisted solvothermal method. Particularly, ionic liquid is utilized for an in situ synthesis of rare-earth-doped binary fluorides on to the graphene oxide. One of the preferred ionic liquids used is 1-butyl-3-methylimidazolium tetrafluoroborate $[C_4mim][BF_4]$. Here ionic liquid $[C_4mim][BF_4]$ is itself working as a fluoride source, as solvent, and templating agent, that is, all three in one. Certainly, the synthesis methodology described in the present work is new and novel and not reported to the best of our knowledge.

3.4. Optical Properties. Figure 7 illustrates the photoluminescence excitation and emission spectra of the as-prepared RE^{3+}-doped NPs and their NCM counterparts, which are measured at RT. In both the NPs and NCMs,

https://doi.org/10.1021/acsomega.1c06875
ACS Omega 2022, 7, 16906−16916

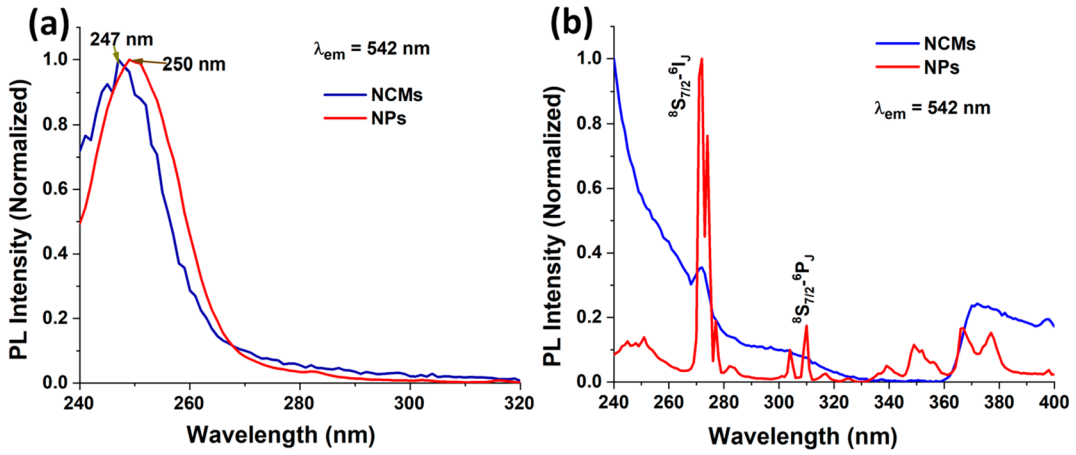

Figure 8. PL excitation spectra: (a) LaF_3:Ce^{3+}/Tb^{3+} NPs (M5) and LaF_3:Ce^{3+}/Tb^{3+}-GO NCMs(M8), (b) GdF_3:Tb^{3+} NPs(M7), and GdF_3:Tb^{3+}-GO NCMs (M10) synthesized by a hydrothermal method using [C_4mim][BF_4] IL.

Ce^{3+} and Gd^{3+} ions are employed as a sensitizer and Tb^{3+} ion as an activator. In the case of Ce^{3+} ions, a broad excitation band is noticed for NPs as well as NCMs due to the 4f-5d electronic transition (shown in Figure 7a,b and Figures 8a and S8c).[54] Interestingly, significant shifting in the normalized excitation peaks of Ce^{3+} ion-doped/based NPs and NCMs is found in different host matrices and in the presence of GO. For instance, two excitation peaks of Ce^{3+} ions appeared at 260 and 287 nm for cubic Ce^{3+} or Ce^{3+}/Tb^{3+} codoped BaF_2 NPs (Figures 7a and S8c). The intense peak at 287 nm is not found to be shifted more than the less intense peak that appeared at 260 nm for BaF_2:Ce^{3+}/Tb^{3+} NPs (M2) and BaF_2:Ce^{3+}/Tb^{3+}-GO NCMs (M4). However, the excitation peak appearing at 260 nm in NPs (M2) is shifted ∼4 nm toward the lower wavelengths NCMs (M4), and it now appears at 256 nm (Figure 7a).

Similar trends of excitation peak shifting in the presence of GO are also found for LaF_3:Ce^{3+}/Tb^{3+}-GO NCMs (M8) and CeF_3:Tb^{3+}-GO (M9) and (Figures 8a and 7b). For example, single broad excitation peaks at 250 and 259 nm are noticed for hexagonal LaF_3:Ce^{3+}/Tb^{3+}(M5) and CeF_3:Tb^{3+}(M6) NPs, respectively. However, in the case of CeF_3:Tb^{3+}-GO NCMs (M9), the excitation peak is considerably shifted 6 nm toward the lower wavelength (now appearing at 253 nm) compared to the CeF_3:Tb^{3+} NPs analogue (M6) in which an excitation peak was found at 259 nm (Figure 7b). Similarly, for LaF_3:Ce^{3+}/Tb^{3+}-GO NCMs (M8), an excitation peak appeared at 247 nm, while in LaF_3:Ce^{3+}/Tb^{3+} NPs (M5), it is observed at 250 nm (Figure 8a). However, there is no change in the excitation ($^8S_{7/2}$-^6I_J) peak position of the Gd^{3+} ion at 272 nm for GdF_3:Tb^{3+} NPs (M7) and GdF_3:Tb^{3+}-GO NCMs (M10) due to an f-f transition (Figure 8b).

In semiconductors, size-dependent photoluminescence properties are found due to the quantum-confinement effect.[55] Consequently, excitation and emission bands are significantly shifted on varying the size of the particles. However, except the Ce^{3+} ion, other RE^{3+}-doped nanoparticles show size-independent photoluminescence behavior due to their f-f electronic transition. Therefore, narrow excitation and emission bands are observed for the rare-earth ions except the Ce^{3+} ion. In the case of Ce^{3+} ions, the 4f-5d transition occurs, which is subject to a crystal field effect. It means that, on varying the crystal field effect, the excitation band may be considerably shifted. It is reported that the Ce^{3+} ion has $^2F_{5/2}$ and $^2F_{7/2}$ as ground states and that the excited level is degenerated ^2D. Ghosh et al. have studied the effect of the ligand field on the photoluminescence behavior of Na-($Y_{1.5}Na_{0.5}$)F_6:Ce (1). They found that the excitation pattern of Ce^{3+} ions is significantly varied in the presence of strongly hydrogen-bonded interlayered/confined water in a layered structure.[56] Since strongly hydrogen-bonded, interlayered water molecules generate a stronger crystal field on the Ce^{3+} ion, a degenerated ^2D excited level is further split, leading to different excited levels. We herein assumed that same situation might also be there in the presence of graphene oxide in the nanocomposite. As the reduced graphene oxide attaches to the surface of Ce^{3+}-doped binary fluorides, it (GO) can enhance the crystal field strength, which leads to the splitting as well as shifting of the excitation peak to a higher energy side. Similarly, Reeves et al. reported the optical properties of CdF_2−CaF_2 superlattices using synchrotron spectroscopy of confined carriers and measured the exciton emission.[55] Also in their experiment they have mentioned the exciton confinement phenomenon.

To get better insight on the effect of GO on the emission of NPs, NPs are excited at their corresponding excitation wavelength as previously discussed. On the one hand, by exciting the bare NPs and NCMs with either Ce^{3+}, Ce^{3+}/Tb^{3+}-doped, or Ce^{3+}-based samples, a broad emission peak of Ce^{3+} ions appears due to the 4d-5f transition, which is susceptible to the external environment. On the other hand, narrow emission bands of Tb^{3+} ions appear at 489, 541, 585, and 620 nm, and these correspond to the transitions from $^5D_4$ to $^7F_6$, $^7F_5$, $^7F_4$, and $^7F_3$, respectively.

The intensity of only Ce^{3+}-doped or Ce^{3+}/Tb^{3+} codoped BaF_2 NPs (M1 and M2) and BaF_2:Ce^{3+}-GO or BaF_2:Ce^{3+}/Tb^{3+}-GO NCMs (M3 and M4) is significantly governed by the excitation wavelength and presence of GO. For example, the intensity of the broad emission peak appearing in bare and doped BaF_2NPs is not only found more intense upon exciting at 287 nm [appearing at 328 nm (M1 and M2)] as compared to the excitation at 260 nm [(341 (M1)/335 nm (M2)] but also the emission peak is shifted toward a lower wavelength on varying the excitation wavelength (Figures S8a and S9a). This might be attributed to the excitation peak at 287 nm being stronger than the excitation peak of 260 nm. Under similar measurement conditions, the emission intensity of Ce^{3+} or Tb^{3+} ions in NCMs is considerably quenched in the presence

https://doi.org/10.1021/acsomega.1c06875
ACS Omega 2022, 7, 16906−16916

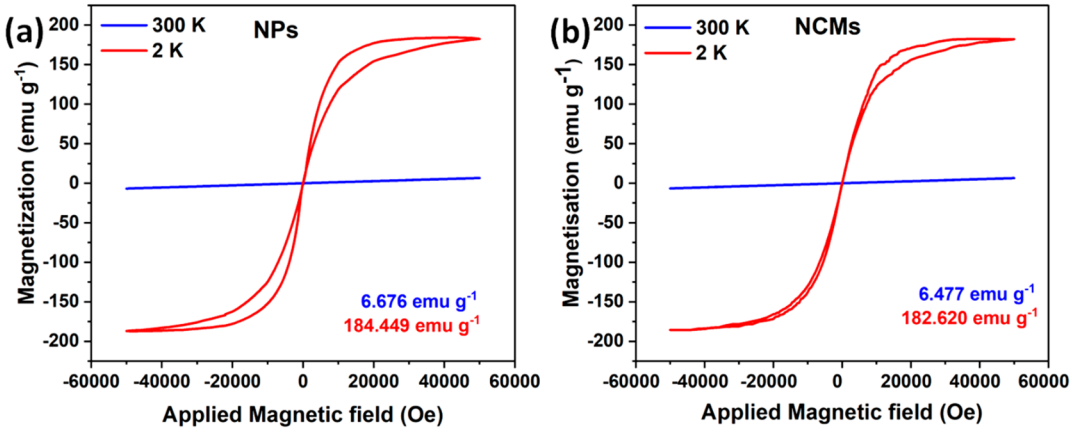

Figure 9. Magnetization vs applied magnetic field plot. (a) GdF_3:Tb^{3+} NPs(M7) and (b) GdF_3:Tb^{3+}-GO NCMs (M10) measured at 300 and 2 K.

of GO (Figure 7c). But, on increasing the slit width up to twofold, emission intensities of Ce^{3+} and Tb^{3+} are significantly increased (but still less intense than the emission intensity of bare NPs in all NCMs). It is also noticed that the emission peak of Ce^{3+} ions in the BaF_2:Ce^{3+}-GO (M3) and BaF_2:Ce^{3+}/Tb^{3+}-GO(M4) NCMs are considerably shifted toward higher energy as compared to their NP analogues (Figures S8b, S9b, and S10b). In another sample, the emission intensity of Tb^{3+} ions in CeF_3:Tb^{3+}-GO (M9) NCMs is significantly more quenched than the bare CeF_3:Tb^{3+} (M6) NPs on using the same slit width (Figure 7d). However, on increasing the twofold slit width, the emission intensity of CeF_3:Tb^{3+}-GO NCMs (M9) is substantially enhanced, and the emission intensity is even close to that of bare NPs, as shown in the inset of Figure 7d. Likewise, the emission intensity of Tb^{3+} ions in the LaF_3:Ce^{3+}/Tb^{3+}-GO(M8) NCMs is also significantly quenched than that of bare LaF_3:Ce^{3+}/Tb^{3+} (M5) NPs, whereas on increasing the slit width their emission intensity is increased to some extent. When a Gd^{3+} ion in GdF_3:Tb^{3+}(M7) NPs and GdF_3:Tb^{3+}-GO (M10) NCMs is excited at 272 nm ($^8S_{7/2}$-^6I_J), then energy transfer takes place from excited Gd^{3+} ions to Tb^{3+} ions. And then by a nonradiative process, energy is relaxed to the $^5D_4$ excited states leading to a $^5D_4$-$^7F_5$ transition.[42] As a result, a highly intense peak is observed in the green region at 542 nm (Figure S9c). The green color luminescence is observed when as-prepared BaF_2:Ce^{3+}/Tb^{3+}-GO (M4) and CeF_3:Tb^{3+}-GO (M9) NCMs are also illuminated at 254 nm using a 6 W UV lamp as shown in Figure 7e,f.

3.5. Magnetic Properties. Additionally, since the Gd^{3+} ions have seven unpaired electrons, the paramagnetic characteristic of Gd^{3+} ions in the GdF_3:Tb NPs (M7) and GdF_3:Tb-GO NCMs (M10) are studied at room temperature (300 K) and low temperature (2 K), since the magnetization is a function of the applied magnetic field (−50 to +50 kOe), as shown in Figure 9. At 300 K, the magnetization (emu g^{-1}) of the M7 (NPs) and M10 (NCMs) samples is found to be 6.676 and 6.477 emu g^{-1} (Figure 9). This means that no significant loss of magnetization of nanoparticles in the presence of GO is found. At a very low temperature (2 K), the magnetization is increased to many folds for the samples GdF_3:Tb NPs (M7) and GdF_3:Tb-GO NCMs (M10) due to the decrease in thermal fluctuation. In this case, the magnetization is found to be 184.449 and 182.620 emu g^{-1} for as-prepared GdF_3:Tb NPs and GdF_3:Tb-GO NCMs, respectively (Figure 9).

Besides this, comparing to other existing literature and to the best of our knowledge, we have reported the maximum magnetization for GdF_3 nanoparticles and their nanocomposites with GO in the same range of applied magnetic field, as shown in Table 2.[57−59] For example, Guan et al. reported 3 emu g^{-1} magnetization at 300 K for the GdF_3:2%Dy^{3+},2%Tb^{3+}, 2% Eu^{3+} nanoparticles; however, GdF_3:Tb^{3+} NPs and GdF_3:Tb^{3+}-GO NCMs reported in the present work show 4.015 and 3.879 emu g^{-1} magnetization in the applied magnetic field from −30 to +30 kOe (Table 2).[56] A similar trend is observed for a low-temperature measurement too at 2 K (Table 2). Furthermore, the high magnetization of the GdF_3:Tb^{3+} NPs and GdF_3:Tb^{3+}-GO NMCs promise their potential use in a biomedical application like MRI imaging, etc.[60,61] In addition, as NPs and NCMs show the maximum magnetization at the high applied magnetic field at RT as well as at a low temperature, these may also be applied for a cryogenic magnetic coolant.[62]

Table 2. Comparison of the Magnetization and Applied Magnetic Field of GdF_3:RE^{3+} Nanoparticles

S. No.	nanoparticles	magnetization (emu/g) 300 K	magnetization (emu/g) 2 K	applied magnetic field	refs
1.	GdF_3:2%Dy^{3+}, 2% Tb^{3+}, 2% Eu^{3+}	3	138	−30 to +30 kOe	56
2.	GdF_3:23%Yb^{3+},1% Tm^{3+}	2	not measured	−20 to 20 kOe	54
3.	GdF_3:Eu^{3+} nanoparticles	2	measured at 77K	−20 to 20 kOe	55
4.	GdF_3:Tb^{3+} nanoparticles	6.676	184.449	−50 to 50 kOe	this work
5.	GdF_3:Tb^{3+}-GO NCMs	6.477	182.620	−50 to 50 kOe	this work
6.	GdF_3:Tb^{3+} nanoparticles	4.015	182.856	−30 to 30 kOe	this work
7.	GdF_3:Tb^{3+}-GO NCMs	3.879	180.517	−30 to 30 kOe	this work
8.	GdF_3:Tb^{3+} nanoparticles	2.674	177.269	−20 to 20 kOe	this work
9.	GdF_3:Tb^{3+}-GO NCMs	2.58	171.091	−20 to 20 kOe	this work

https://doi.org/10.1021/acsomega.1c06875
ACS Omega 2022, 7, 16906−16916

4. CONCLUSIONS

In summary, a new class (any lanthanide ion as dopant or host can be used) of novel NCMs of RE^{3+}-doped binary fluorides with GO have been synthesized using the $[C_4mim][BF_4]$ IL-assisted hydrothermal method where IL is used as a solvent, templating agent, and a reaction partner, that is, all three in one. No other solvent is used except water in the synthesis. It is found that GO also acts as a templating agent along with IL in the synthesis of NCMs. In the presence of GO, for all the cases, not only is the crystallite size reduced but also lattice strain is significantly tuned. As an example, the crystallite size for the CeF_3:Tb nanoparticle is found at 38.6 nm; however, CeF_3:Tb-GO shows the crystallite size of 20.0 nm. Interestingly, it is observed for the first time that optical properties, especially excitation and emission spectra of Ce^{3+} ions, are considerably tuned in the presence of GO; especially, excitation spectra of the Ce^{3+} ion are shifted to higher energy. For example, an excitation peak is observed at 259 nm for CeF_3:Tb nanoparticles; however, it is shifted to 6 nm for CeF_3:Tb-GO nanocomposites. Though the emission intensity decreases for the nanocomposites, it shows a high luminescence property, which is promising for the application of NCMs in various photonic/biphotonic fields. In addition, the GO part of the nanocomposite can be useful for suitable applications too. GdF_3:Tb^{3+} NPs and their NCM analogues with GO (GdF_3:Tb^{3+}-GO) have revealed maximum magnetization; therefore, these can also be employed as a potential candidate for imaging and cryogenic magnetic coolant, etc.

■ ASSOCIATED CONTENT

Supporting Information

The Supporting Information is available free of charge at https://pubs.acs.org/doi/10.1021/acsomega.1c06875.

Chemical details, synthesis detail (graphene oxide), NMR of ILs, FTIR (IL, nanoparticles, and nanocomposites); Raman spectra of GO, characterization techniques, PXRD patterns, lattice strain, FESEM and TEM images of as-prepared nanoparticles; photoluminescence spectra of nanoparticles and nanocomposites, magnetic properties detail of nanoparticles and nanocomposites (PDF)

■ AUTHOR INFORMATION

Corresponding Author

Pushpal Ghosh − *Department of Chemistry, Dr. H.S. Gour University (A Central University), Sagar 470003 Madhya Pradesh, India;* orcid.org/0000-0002-7596-5056; Email: pusphalghosh27@gmail.com, pghosh@dhsgsu.edu.in

Authors

Rahul Kumar Sharma − *Department of Chemistry, Dr. H.S. Gour University (A Central University), Sagar 470003 Madhya Pradesh, India; Department of Chemistry, Government Shyam Sundar Agrawal PG College, Jabalpur 483225 Madhya Pradesh, India*

Madhubrata Ghora − *Department of Chemistry, Dr. H.S. Gour University (A Central University), Sagar 470003 Madhya Pradesh, India*

Yogendra N. Chouryal − *Department of Chemistry, Dr. H.S. Gour University (A Central University), Sagar 470003 Madhya Pradesh, India*

Trisit Ganguly − *Department of Chemistry, Dr. H.S. Gour University (A Central University), Sagar 470003 Madhya Pradesh, India*

Debopam Acharjee − *Department of Chemistry, Dr. H.S. Gour University (A Central University), Sagar 470003 Madhya Pradesh, India*

Dibya Jyoti Mondal − *Department of Chemistry, Indian Institute of Science Education and Research Bhopal, Bhopal 462066 Madhya Pradesh, India*

Sanjit Konar − *Department of Chemistry, Indian Institute of Science Education and Research Bhopal, Bhopal 462066 Madhya Pradesh, India;* orcid.org/0000-0002-1584-6258

Sandeep Nigam − *Chemistry Division, Bhabha Atomic Research Centre, Trombay 400085 Mumbai, India;* orcid.org/0000-0001-9949-4466

Complete contact information is available at: https://pubs.acs.org/10.1021/acsomega.1c06875

Notes

The authors declare no competing financial interest.

■ ACKNOWLEDGMENTS

We are grateful to the Science and Engineering Research Board, Government of India (Core Research Grant), for funding. Authors acknowledge Sophisticated Instrumentation Cenrte (SIC) of Dr. H. S. Gour University and Department of Chemistry for characterization facility.

■ REFERENCES

(1) Dhonde, M.; Sahu, K.; Murty, V. V. S. Cu-Doped TiO_2 Nanoparticles/Graphene Composites for Efficient Dye-Sensitized Solar Cells. *Sol. Energy* **2021**, *220*, 418−424.

(2) Torkashv and, N.; Sarlak, N. Polymerized Graphene Oxide/$MnCe_{0.5}Fe_{1.5}O_4$ Nanoferrofluid as a T2- and T2*-Weighted Contrast Agent for Magnetic Resonance Imaging. *Colloids Surfaces B Biointerfaces* **2020**, *185*, 110555.

(3) Saravanan, T.; Anandan, P.; Shanmugam, M.; Azhagurajan, M.; Mohamed Ismail, M.; Arivanandhan, M.; Hayakawa, Y.; Jayavel, R. Facile Synthesis of Yb_2O_3−Graphene Nanocomposites for Enhanced Energy and Environmental Applications. *Polym. Bull.* **2020**, *77* (8), 3891−3906.

(4) Kim, I.; Park, S. W.; Kim, D. W. Onion-like Crystalline WS_2 Nanoparticles Anchored on Graphene Sheets as High-Performance Anode Materials for Lithium-Ion Batteries. *Chem. Eng. J.* **2019**, *375*, 122033.

(5) Lingamdinne, L. P.; Koduru, J. R.; Chang, Y. Y.; Kang, S. H.; Yang, J. K. Facile Synthesis of Flowered Mesoporous Graphene Oxide-Lanthanum Fluoride Nanocomposite for Adsorptive Removal of Arsenic. *J. Mol. Liq.*. **2019**, *279*, 32−42.

(6) Sun, J.; Song, L.; Fan, Y.; Tian, L.; Luan, S.; Niu, S.; Ren, L.; Ming, W.; Zhao, J. Synergistic Photodynamic and Photothermal Antibacterial Nanocomposite Membrane Triggered by Single NIR Light Source. *ACS Appl. Mater. Interfaces* **2019**, *11* (30), 26581−26589.

(7) Jafari, H.; Ganjali, M. R.; Shiralizadeh Dezfuli, A.; Kohan, E. A Platform for Electrochemical Sensing of Biomolecules Based on Europia/Reduced Graphene Oxide Nanocomposite. *J. Mater. Sci. Mater. Electron.* **2018**, *29* (24), 20639−20649.

(8) Dezfuli, A. S.; Ganjali, M. R.; Naderi, H. R. Anchoring Samarium Oxide Nanoparticles on Reduced Graphene Oxide for High-Performance Supercapacitor. *Appl. Surf. Sci.*. **2017**, *402*, 245−253.

(9) Ojha, G. P.; Pant, B.; Park, S. J.; Park, M.; Kim, H. Y. Synthesis and Characterization of Reduced Graphene Oxide Decorated with

CeO_2-Doped MnO_2 Nanorods for Supercapacitor Applications. *J. Colloid Interface Sci.*. **2017**, *494*, 338−344.
(10) Bera, R.; Kundu, S.; Patra, A. 2D Hybrid Nanostructure of Reduced Graphene Oxide-CdS Nanosheet for Enhanced Photocatalysis. *ACS Appl. Mater. Interfaces* **2015**, *7* (24), 13251−13259.
(11) Meng, F.; Li, J.; Cushing, S. K.; Bright, J.; Zhi, M.; Rowley, J. D.; Hong, Z.; Manivannan, A.; Bristow, A. D.; Wu, N. Photocatalytic Water Oxidation by Hematite/Reduced Graphene Oxide Composites. *ACS Catal.* **2013**, *3* (4), 746−751.
(12) Wang, Y.; Wang, H.; Liu, D.; Song, S.; Wang, X.; Zhang, H. Graphene Oxide Covalently Grafted Upconversion Nanoparticles for Combined NIR Mediated Imaging and Photothermal/Photodynamic Cancer Therapy. *Biomaterials* **2013**, *34* (31), 7715−7724.
(13) Wang, W.; Huang, W.; Ni, Y.; Lu, C.; Tan, L.; Xu, Z. Graphene Supported $BaYF_4$:Yb^{3+},Tm^{3+} and N Doped P25 Nanocomposite as an Advanced NIR and Sunlight Driven Upconversion Photocatalyst. *Appl. Surf. Sci.*. **2013**, *282*, 832−837.
(14) Wei, W.; He, T.; Teng, X.; Wu, S.; Ma, L.; Zhang, H.; Ma, J.; Yang, Y.; Chen, H.; Han, Y.; et al. Nanocomposites of Graphene Oxide and Upconversion Rare-Earth Nanocrystals with Superior Optical Limiting Performance. *Small* **2012**, *8* (14), 2271−2276.
(15) Li, Y.; Wang, G.; Pan, K.; Jiang, B.; Tian, C.; Zhou, W.; Fu, H. NaYF4:Er3+/Yb3+-Graphene Composites: Preparation, Upconversion Luminescence, and Application in Dye-Sensitized Solar Cells. *J. Mater. Chem.* **2012**, *22* (38), 20381−20386.
(16) Wang, Y.; Li, Z.; Hu, D.; Lin, C. T.; Li, J.; Lin, Y. Aptamer/Graphene Oxide Nanocomplex for in Situ Molecular Probing in Living Cells. *J. Am. Chem. Soc.* **2010**, *132* (27), 9274−9276.
(17) Tao, Y.; Lin, Y.; Huang, Z.; Ren, J.; Qu, X. Incorporating Graphene Oxide and Gold Nanoclusters: A Synergistic Catalyst with Surprisingly High Peroxidase-like Activity over a Broad PH Range and Its Application for Cancer Cell Detection. *Adv. Mater.* **2013**, *25* (18), 2594−2599.
(18) Wang, H.; Yuan, X.; Wu, Y.; Huang, H.; Peng, X.; Zeng, G.; Zhong, H.; Liang, J.; Ren, M. M. Graphene-Based Materials: Fabrication, Characterization and Application for the Decontamination of Wastewater and Wastegas and Hydrogen Storage/Generation. *Adv. Colloid Interface Sci.* **2013**, *195*−*196*, 19−40.
(19) Geim, A. K.; Novoselov, K. S. The Rise of Graphene. *Nanosci. Technol. A Collect. Rev. from Nat. Journals* **2009**, 11−19.
(20) Liu, J. W.; Zhang, Y.; Chen, X. W.; Wang, J. H. Graphene Oxide-Rare Earth Metal-Organic Framework Composites for the Selective Isolation of Hemoglobin. *ACS Appl. Mater. Interfaces* **2014**, *6* (13), 10196−10204.
(21) Ju, B.; Wang, X.; Wu, C.; Yang, X.; Shu, H.; Bai, Y.; Wen, W.; Yi, X. Electrochemical Performance of the Graphene/Y_2O_3/$LiMn_2O_4$ Hybrid as Cathode for Lithium-Ion Battery. *J. Alloys Compd.*. **2014**, *584*, 454−460.
(22) Zheng, L.; Cheng, X.; Cao, D.; Zhang, D.; Wang, Z.; Xu, D.; Xia, C.; Shen, L.; Yu, Y. Al_2O_3-Gd_2O_3 Double-Films Grown on Graphene Directly by H_2O-Assisted Atomic Layer Deposition. *RSC Adv.* **2014**, *4* (83), 44296−44301.
(23) Yang, S.; Gao, H.; Wang, Y.; Xin, S.; He, Y.; Wang, Y.; Zeng, W. A Simple Way to Synthesize Well-Dispersed Gd_2O_3 Nanoparticles onto Reduced Graphene Oxide Sheets. *Mater. Res. Bull.* **2013**, *48* (1), 37−40.
(24) Mo, Z.; Zhao, Y.; Guo, R.; Liu, P.; Xie, T. Preparation and Characterization of Graphene/Europium Oxide Composites. *Mater. Manuf. Process.* **2012**, *27* (5), 494−498.
(25) Gupta, B. K.; Thanikaivelan, P.; Narayanan, T.; et al. Optical Bifunctionality of Europium-Complexed Luminescent Graphene Nanosheets. *Nano Lett.* **2011**, *11* (12), 5227−5233.
(26) Cao, Y.; Yang, T.; Feng, J.; Wu, P. Decoration of Graphene Oxide Sheets with Luminescent Rare-Earth Complexes. *Carbon N. Y.* **2011**, *49* (4), 1502−1504.
(27) Yang, X.; Li, Z.; Ju, E.; Ren, J.; Qu, X. Reduced Graphene Oxide Functionalized with a Luminescent Rare-Earth Complex for the Tracking and Photothermal Killing of Drug-Resistant Bacteria. *Chem. - A Eur. J.* **2014**, *20* (2), 394−398.
(28) Li, Z.; Johnson, O.; Huang, J.; Feng, T.; Yang, C.; Liu, Z.; Chen, W. Enhancing the Photothermal Conversion Efficiency of Graphene Oxide by Doping with $NaYF_4$: Yb, Er Upconverting Luminescent Nanocomposites. *Mater. Res. Bull.* **2018**, *106* (March), 365−370.
(29) Wang, W.; Li, Y.; Kang, Z.; Wang, F.; Yu, J. C. A NIR-Driven Photocatalyst Based on α-$NaYF_4$: YB,Tm@TiO_2 Core-Shell Structure Supported on Reduced Graphene Oxide. *Appl. Catal. B Environ.*. **2016**, *182*, 184−192.
(30) Bai, S.; Shen, X. Graphene-Inorganic Nanocomposites. *RSC Adv.* **2012**, *2* (1), 64−98.
(31) Singh, R.; Kumar, M.; Khajuria, H.; Sharma, S.; Sheikh, H. N. Studies on Hydrothermal Synthesis of Photolumniscent Rare Earth (Eu^{3+} & Tb^{3+}) Doped NG@$FeMoO_4$ for Enhanced Visible Light Photodegradation of Methylene Blue Dye. *Solid State Sci.*. **2018**, *76*, 38−47.
(32) Plechkova, N. V.; Seddon, K. R. Applications of Ionic Liquids in the Chemical Industry. *Chem. Soc. Rev.* **2008**, *37* (1), 123−150.
(33) Earle, M. J.; Seddon, K. R. Ionic Liquids: Green Solvents for the Future. *ACS Symp. Ser.* **2002**, *819* (7), 10−25.
(34) Duan, X.; Ma, J.; Lian, J.; Zheng, W. The Art of Using Ionic Liquids in the Synthesis of Inorganic Nanomaterials. *CrystEngComm* **2014**, *16* (13), 2550−2559.
(35) Fonseca, G. S.; Umpierre, A. P.; Fichtner, P. F. P.; Teixeira, S. R.; Dupont, J. The Use of Imidazolium Ionic Liquids for the Formation and Stabilization of Ir0 and Rh0 Nanoparticles: Efficient Catalysts for the Hydrogenation of Arenes. *Chem. - A Eur. J.* **2003**, *9* (14), 3263−3269.
(36) Lian, J.; Duan, X.; Ma, J.; Peng, P.; Kim, T.; Zheng, W. Hematite (α - -Fe $_2$ O $_3$) with Various Morphologies: Ionic Liquid-Assisted Synthesis, Formation Mechanism, and Properties. *ACS Nano* **2009**, *3* (11), 3749−3761.
(37) Alammar, T.; Noei, H.; Wang, Y.; Mudring, A. V. Mild yet Phase-Selective Preparation of TiO_2 Nanoparticles from Ionic Liquids-a Critical Study. *Nanoscale* **2013**, *5* (17), 8045−8055.
(38) Ghosh, P.; Mudring, A. V. Phase Selective Synthesis of Quantum Cutting Nanophosphors and the Observation of a Spontaneous Room Temperature Phase Transition. *Nanoscale* **2016**, *8* (15), 8160−8169.
(39) Cybińska, J.; Lorbeer, C.; Mudring, A. V. Phosphate Protected Fluoride Nano-Phosphors. *J. Mater. Chem.* **2012**, *22* (19), 9505−9508.
(40) Zhang, C.; Chen, J.; Zhou, Y.; Li, D. Ionic Liquid-Based " All-in-One " Synthesis and Photoluminescence Properties of Lanthanide Fluorides. *J. Phys. Chem. C* **2008**, *112*, 10083−10088.
(41) Sharma, R. K.; Chouryal, Y. N.; Ghosh, P.; Slesarev, A. I.; Ivanovskikh, K. V.; Leonidov, I. I.; Nigam, S. A Closer Look at the Defects and Luminescence of Nanocrystalline Fluorides Synthesized Via Ionic Liquids: The Case of Ce^{3+}-Doped BaF_2. *New J. Chem.* **2020**, *44* (1), 200−209.
(42) Lorbeer, C.; Mudring, A. V. Quantum Cutting in Nanoparticles Producing Two Green Photons. *Chem. Commun.* **2014**, *50* (87), 13282−13284.
(43) Sharma, R. K.; Chouryal, Y. N.; Chaudhari, S.; Saravanakumar, J.; Dey, S. R.; Ghosh, P. Adsorption-Driven Catalytic and Photocatalytic Activity of Phase Tuned In $_2$ S $_3$ Nanocrystals Synthesized via Ionic Liquids. *ACS Appl. Mater. Interfaces* **2017**, *9*, 11651−11661.
(44) Lorbeer, C.; Cybińska, J.; Mudring, A. V. Europium(III) Fluoride Nanoparticles from Ionic Liquids: Structural, Morphological, and Luminescent Properties. *Cryst. Growth Des.* **2011**, *11* (4), 1040−1048.
(45) Ghosh, P.; Sharma, R. K.; Chouryal, Y. N.; Mudring, A. V. Size of the Rare-Earth Ions: A Key Factor in Phase Tuning and Morphology Control of Binary and Ternary Rare-Earth Fluoride Materials. *RSC Adv.* **2017**, *7* (53), 33467−33476.
(46) Sharma, R. K.; Ghosh, P. Lanthanide-Doped Luminescent Nanophosphors via Ionic Liquids. *Front. Chem.* **2021**, *9*, 1−26.
(47) Chouryal, Y. N.; Sharma, R. K.; Acharjee, D.; Ganguly, T.; Pandey, A.; Ghosh, P. Influence of Ionic Liquids and Concentration

https://doi.org/10.1021/acsomega.1c06875
ACS Omega 2022, 7, 16906−16916

of Red Phosphorous on Luminescent Cu3P Nanocrystals. *J. Chem. Sci.* **2019**, *131* (9). DOI: 10.1007/s12039-019-1665-y.
(48) Zheng, W.; Liu, X.; Yan, Z.; Zhu, L. Ionic Liquid-Assisted Synthesis of Large-Scale TiO Nanoparticles with Controllable Phase by Hydrolysis of TiCl. *ACS Nano* **2009**, *3*, 115−122.
(49) Zhou, Y.; Antonietti, M. Synthesis of Very Small TiO_2 Nanocrystals in a Room-Temperature Ionic Liquid and Their Self-Assembly toward Mesoporous Spherical Aggregates. *J. Am. Chem. Soc.* **2003**, *125* (49), 14960−14961.
(50) Chen, H.; Dong, S. Self-Assembly of Ionic Liquids-Stabilized Pt Nanoparticles into Two-Dimensional Patterned Nanostructures at the Air-Water Interface. *Langmuir* **2007**, *23* (25), 12503−12507.
(51) Singh, T.; Kumar, A. Aggregation Behavior of Ionic Liquids in Aqueous Solutions : Effect of Alkyl Chain Length, Cations, and Anions Aggregation Behavior of Ionic Liquids in Aqueous Solutions : Effect of Alkyl Chain Length, Cations, and Anions. *J. Phys. Chem. B* **2007**, *111*, 7843−7851.
(52) Wu, S.; Duan, N.; Ma, X.; Xia, Y.; Wang, H.; Wang, Z.; Zhang, Q. Multiplexed Fluorescence Resonance Energy Transfer Aptasensor between Upconversion Nanoparticles and Graphene Oxide for the Simultaneous Determination of Mycotoxins. *Anal. Chem.* **2012**, *84* (14), 6263−6270.
(53) Malik, M.; Padhye, P.; Poddar, P. Graphene Quantum Dots-Driven Multiform Morphologies of β-$NaYF_4$:Gd^{3+}/Tb^{3+} Phosphors: The Underlying Mechanism and Their Optical Properties. *ACS Omega* **2018**, *3* (2), 1834−1849.
(54) Ghosh, P.; Kar, A.; Patra, A. Energy Transfer Study between Ce^{3+} and Tb^{3+} Ions in Doped and Core-Shell Sodium Yttrium Fluoride Nanocrystals. *Nanoscale* **2010**, *2* (7), 1196−1202.
(55) Ivanovskikh, K. V.; Hughes-Currie, R. B.; Reid, M. F.; Wells, J. P. R.; Sokolov, N. S.; Reeves, R. J. Synchrotron Spectroscopy of Confined Carriers in CdF_2-CaF_2 Superlattices. *J. Appl. Phys.* **2016**, *119* (10), 1−6.
(56) Ghosh, P.; Kar, A.; Patra, A. Structural Changes and Spectroscopic Properties of Ce $^{3+}$ -Ion-Doped Sodium Yttrium Fluoride Nanocrystals : Influences of Sonication and Temperature. *J. Phys. Chem. C* **2010**, *114*, 715−722.
(57) Wong, H.-T.; Chan, H. L. W.; Hao, J. Towards Pure Near-Infrared to near-Infrared Upconversion of Multifunctional GdF_3:Yb^{3+},Tm^{3+} Nanoparticles. *Opt. Express* **2010**, *18* (6), 6123.
(58) Wong, H. T.; Chan, H. L. W.; Hao, J. H. Magnetic and Luminescent Properties of Multifunctional GdF_3: Eu^{3+} Nanoparticles. *Appl. Phys. Lett.* **2009**, *95* (2), 1−4.
(59) Guan, H.; Sheng, Y.; Xu, C.; Dai, Y.; Xie, X.; Zou, H. Energy Transfer and Tunable Multicolor Emission and Paramagnetic Properties of GdF_3:Dy^{3+}, Tb^{3+}, Eu^{3+} Phosphors Hongxia. *Phys. Chem. Chem. Phys.* **2016**, *18*, 19807−19819.
(60) Rodriguez-Liviano, S.; Nuñez, N. O.; Rivera-Fernández, S.; De La Fuente, J. M.; Ocaña, M. Ionic Liquid Mediated Synthesis and Surface Modification of Multifunctional Mesoporous Eu:GdF_3 Nanoparticles for Biomedical Applications. *Langmuir* **2013**, *29* (10), 3411−3418.
(61) Passuello, T.; Pedroni, M.; Piccinelli, F.; Polizzi, S.; Marzola, P.; Tambalo, S.; Conti, G.; Benati, D.; Vetrone, F.; Bettinelli, M.; et al. PEG-Capped, Lanthanide Doped GdF_3 Nanoparticles: Luminescent and T2 Contrast Agents for Optical and MRI Multimodal Imaging. *Nanoscale* **2012**, *4* (24), 7682−7689.
(62) Chen, Y. C.; Prokleška, J.; Xu, W. J.; Liu, J. L.; Liu, J.; Zhang, W. X.; Jia, J. H.; Sechovský, V.; Tong, M. L. A Brilliant Cryogenic Magnetic Coolant: Magnetic and Magnetocaloric Study of Ferromagnetically Coupled GdF3. *J. Mater. Chem. C* **2015**, *3* (47), 12206−12211.

https://doi.org/10.1021/acsomega.1c06875
ACS Omega 2022, 7, 16906−16916